Title

Corrosion of carbon steel and the passivating properties of corrosion films formed under high-PT geothermal conditions

Authors

Mundhenk, Niklas

Knauss, Kevin G

Bandaru, Siva RS

et al.

Publication Date

2019-08-01

DOI

10.1016/j.scitotenv.2019.04.386

Peer reviewed

Corrosion of carbon steel and the passivating properties of corrosion films formed under high-PT geothermal conditions

Niklas Mundhenk*[1], Kevin G. Knauss[1], Siva R. S. Bandaru[2], Robert Wonneberger[3], Thomas M. Devine[2]

[1]Energy Geosciences Division, Lawrence Berkeley National Laboratory, Berkeley, California 94720, United States

[2]University of California, Berkeley, California 94720, United States

[3]Otto Schott Institute of Materials Research at the Friedrich Schiller University of Jena, 07743 Jena, Germany

Abstract

Corrosion is a major obstacle to a safe implementation of geotechnical applications. Using a novel approach that includes vertical scanning interferometry (VSI) and electrochemical impedance spectroscopy (EIS) we discuss time-dependent carbon steel corrosion and film formation at geothermally relevant temperatures (80-160°C) in CO_2-saturated mildly acidic Na-Cl brine. Iron dissolution kinetics follows a logarithmic rate at 80 and 160°C and a linear rate at 120°C. At 80°C, high initial corrosion rates (first 24 hours) generate H_2 at a minimum rate of 12 µmol h^{-1} cm^{-2} and lead to the formation of a continuous ~100 µm thick porous corrosion film. It exhibits a duplex structure with a crystalline outer $FeCO_3$ layer and an inner layer composed of a skeletal network of Fe_3C impregnated with $FeCO_3$. Being an electrical conductor we hypothesize the Fe_3C to strongly enhance corrosion rates by providing additional cathodic sites. Pseudo-passivity due to an anodic film-forming reaction (presumably Fe-oxide) was observed at 120 and 160°C, soon followed by the initiation of pitting at 120°C. Steady-state corrosion rates at 160°C are at least one order of magnitude lower than for 120°C. Our experimental approach demonstrated potential for general applicability in studying corrosion-related phenomena.

Introduction

An increased use of the deeper subsurface has given the field of material corrosion in geological environments (high P-T conditions) a new timeliness and also merged the fields of corrosion science and geochemistry. Recent studies focusing on corrosion in nuclear waste disposal (NWD; Feron et al., 2008; Lee et al., 2006; Schlegel et al., 2010; Schütz et al., 2015;), CO_2 sequestration (Choi et al., 2010; Pfennig & Bässler, 2009), and the utilization of geothermal energy (Mundhenk et al., 2013; Mundhenk et al., 2014) acknowledged that material degradation on casings, pipelines, or containers can have severe consequences, such as groundwater contamination and

release/accumulation of radionuclides into the environment. Furthermore, corrosion-induced hydrogen gas production can lead to significant pressure build-up and damage low-permeable geologic clay repositories in NWD (Feron et al., 2008). Assuring material integrity and/or having a good estimate for corrosion kinetics are therefore essential for a successful and safe implementation of geotechnical applications.

Geothermal fluids are inevitably corrosive, arising from the combination of high temperatures and the presence of corrosive key species, e.g. chloride ions and/or dissolved CO_2 (Ellis & Mahon, 1977). However, scale-forming solutes are present in typical geothermal fluids and lead to the formation of a corrosion film incorporating anodically released Fe cations. The corrosion film is important in different respects: (i) it can slow down corrosion substantially (Banas et al., 2007; Mundhenk et al., 2013; Nesic, 2007), (ii) its properties determine which type of corrosion will occur, and (iii) it can provide a sink for potentially toxic and radioactive scale minerals, such as barite and galena (Scheiber et al., 2014).

Temperature is the main driver that accelerates all the processes involved in corrosion systems: electrochemical, chemical, and transport (Nesic et al., 2007). It also determines which Fe phases are thermodynamically stable to form the film. Under geothermal conditions siderite ($FeCO_3$) is often encountered due to the presence of CO_2 and the absence of O_2. Such films undergo pronounced changes as a function of temperature and formation time (Blengino et al., 1995; Gao et al., 2011; Han et al., 2011; Nesic et al., 2007; Zhang et al., 2012) and often have an internal layer structure (Gao et al., 2011). Nesic characterized $FeCO_3$ films and described an interplay between corrosion and scaling in which scale formation kinetically competes with corrosion to fill the voids left behind[12]. Others found $FeCO_3$ to promote conditions at the metal/film interface under which oxide passive films are thermodynamically stable and significantly contribute to corrosion resistance (Han et al., 2011; Tanupabrungsun et al., 2013). When corrosion resistance relies on an oxide film, however, localized corrosion becomes more likely which is a more severe form of corrosion.

Little is known about the corrosion and film formation at geothermally-relevant temperatures exceeding 100°C. Existing research is often ambiguous as to whether corrosion intensifies as temperature increases, mainly due to an incomplete understanding of corrosion film growth and its structural properties. This paper makes use of an array of complementary experimental techniques. We address fundamental properties of evolving corrosion films to decipher the complex corrosion behavior. A comprehensive dynamic on corrosion kinetics and film formation is shown with implications for geotechnical applications in which temperature is a key factor.

Materials and methods

Experimental setup: Experiments have been performed as a function of time (1, 2, 4, 10 days) and temperature (80, 120, and 160°C) in an all-titanium Parr mixed-flow reactor (MFR; 300 ml volume). The flow rate is held constant at 0.2 ml min^{-1} using a Quizix high-P syringe pump, so that the fluid volume in the reactor is exchanged every 25

hours. The fluid is constantly stirred at a rate of 500 rpm. A pressure of 50±4 bar is maintained over the course of the experiment to prevent CO_2 degassing.

Steel sample: Corrosion experiments were conducted with an as-received pipeline steel (API grade P110) often used for deep wells. It has the following composition [wt.%]: C 0.5, Mn 1.1, Si 0.23, Cu 0.1 Fe bal. The high carbon content leads to a ferritic-pearlitic microstructure, in which pearlite is a two-phase mixture consisting of alternating plates of ferrite and Fe_3C. For each experiment two rectangular samples were placed in the reactor: one working electrode (0.25 cm^2) connected to a potentiostat and one sample (2 cm^2) that is freely corroding at the bottom of the reactor. The results reported are from separate experiments conducted for various time durations. A PTFE disc (ø 1mm) was used to mask a portion of the latter sample to have a reference height to measure the corrosion rate after film removal. The PTFE disc was gently pressed against the sample with a Ti jig following the approach by Pollet-Villard (…). Part of the sample was used for SEM/EDX analysis. Before each experiment the samples were sequentially polished up to 1200 grit, rinsed with water, degreased in acetone, and dried.

Post-exposure analysis and surface retreat determination: Vertical scanning interferometry (VSI; Zygo NewView 7300) was used to map the surface topography. Prior to VSI analysis the sample was immersed in inhibited HCl (100 ml HCl (conc.) + 2 g Sb_2O_3 + 5 g $SnCl_2$) to remove the corrosion product. Surface reflectivity was enhanced by applying a sputter deposited Au coating. The topography of the sample was measured and plotted as the altitude distribution so that the volume (per cm^2) removed by corrosion could be measured. Taking into account the exposure time, corrosion rates were calculated. A scanning electron microscope (SEM; Zeiss Evo LS10) equipped with an energy dispersive X-ray (EDX) detector was used for a structural and compositional analysis of the corrosion films (acceleration voltage 15 kV).

Fluid and gas chemistry: The fluid contains 2 M NaCl and 40 mM $NaHCO_3$ solution. It was equilibrated for at least 24 hours in a 4 liter titanium vessel at 10 bar pCO_2 (research-grade). Using PhreeqC with the latest Pitzer database we calculated a solution pH of ~5.1 (at 25°C) and a total carbon concentration of 0.2723 mol kg^{-1} (Parkhurst & Appelo, 1999). Deaeration was achieved by adding the salts under N_2 atmosphere to deionized water (18.2 MΩ·cm) that had been boiled vigorously for 15 minutes. Total aqueous Fe concentrations ($[Fe]_{aq}$) in the effluent were determined using an inductively coupled plasma optical emission spectrometer (ICP-OES; Perkin Elmer 5300DV). Gaseous hydrogen concentration ($[H_2]_g$) was analyzed by gas chromatography (Perkin Elmer Clarus 580 GC) with N_2 as carrier gas. $[H_2]$ has not been corrected for its solubility in the analyzed fluid sample. However, it largely partitions into the gas phase upon GC analysis at atmospheric pressure.

Electrochemical measurements: Electrochemical experiments have been conducted with a standard three-electrode setup with a P110 sample as the working electrode (0.25 cm^2), a Pt mesh counter electrode, and a custom-made (chloridized) Ag/AgCl reference electrode (RE). It was satisfactorily tested against a commercial Ag/AgCl (3M) electrode. Potentiodynamic polarization (PDP) scans (scan rate 1 mV/s) were measured after 1 hour and 10 days for each experiment by polarizing from -250 mV to +250 mV (vs. OCP). During the experiment the

open circuit potential (OCP), the polarization resistance (R_p), and the impedance (EIS) have been measured. In a programmed measurement sequence, first the OCP was measured for 60 min. To measure R_p, LPR tests were conducted by polarizing from -10 to 10 mV vs. OCP with a scan rate of 0.25 mV s^{-1}. R_p (in Ω cm^2) is defined as the slope of the potential-current density ($\Delta E/\Delta i$) curve at the OCP (normalized to 1 cm^2) and is inversely proportional to the corrosion current density. Impedance spectra were recorded at OCP with a sinusoidal potential excitation of 10 mV amplitude from 100 kHz to 2.5 mHz. Kramer-Kronigs analysis was performed after each experiment to confirm the validity of EIS data (causality, linearity, stability).

Results and discussion

Corrosion is an electrochemical process coupling the oxidation of metals (anodic reaction) and the reduction of an oxidizing agent (cathodic reaction) in an electrolyte. In oxygen-free and slightly acidic environments the overall corrosion reaction can be written as

$$\square\square_{(s)} + 2\square_2O_{(l)} \rightarrow \square\square^{2+} + 2\square\square^{-} + \square_{2(\square)} \qquad \text{eq. 1}$$

Fe^{2+} cations and gaseous H_2 are the main products of the electrochemical reaction in which elemental $Fe_{(s)}$ is oxidized in an anodic partial reaction releasing two electrons. Charge neutrality requires the electrons to be consumed in a cathodic reaction which, according to the mixed potential theory, take place simultaneously at the same metal/electrolyte interface. Possible H_2-producing cathodic reactions are the reduction of H^+ and H_2O, which are thermodynamically equivalent, as well as of $CO_{2(aq)}$, and HCO_3^-. However, it has been shown that the latter are thermodynamically unfavorable compared to the more classical $2H^+ + 2e^- \longrightarrow H_2$ reaction (Linter & Burstein, 1999). In addition, the reduction rate of C-containing species is limited by a slow chemical step, the hydration of CO_2 (Nesic et al., 2007). The effect of CO_2 on the anodic reaction is generally smaller, but not negligible. For instance, Kahyarian et al. found a significant enhancement of the anodic reaction rate at pressures as low as 1 bar (Kahyarian et al., 2017).

Electrochemical corrosion is assisted by Cl^- ions ($[Cl^-]$ = 2 mol kg^{-1} in the experimental fluid) which are capable of chemisorbing onto the metal surface, replacing adsorbed water molecules (Landolt, 2007). Cl^- ions adversely interfere with oxide passive films promoting localized corrosion Szklarska-Smialowska, 1986). While the causality between Cl^- ions and localized corrosion is generally accepted, the underlying mechanisms are still matter of debate (Soltis, 2015). Some of the corrosion-relevant properties of the geothermal fluid (e.g. chloride activity, pH) change significantly in the temperature range between 80 to 160°C. Thermodynamic calculations show that the chloride ion activity drops significantly with increasing temperature as more Cl^- ions are bound in an uncharged $NaCl^0$ complex. The pH increases with increasing temperature due to a decrease in CO_2 solubility (5.5 (80°C), 5.8 (120°C), 6.2 (160°C) with potential implications for the solubility of film-forming phases. The metal-electrolyte interface is a highly dynamic local chemical environment that strongly differs from the bulk (Almeida et al., 2018; Han et al., 2011; Ingham et al., 2015; Nesic, 2007). For instance, Han et al. showed that the local pH at the interface can

increase to 9 even if the bulk pH is 4-6, lowering the solubility of Fe phases, including Fe_3O_4 and $FeCO_3$ (Han et al., 2011). Fe_3O_4 typically forms a very thin film, whereas $FeCO_3$ films can grow to considerable thickness.

Vertical scanning interferometry (VSI) measurements

Representative VSI images of sample surfaces after 10 days at different temperatures are given in Fig. 1a-c. At 80 and 160°C, two distinct peaks in the altitude distribution plot can be identified, representing the masked and the corroded portion of the surface. However, in the 80°C case the peaks are well separated and more than 100 times further apart than for 160°C. This type of corrosion can be described as uniform corrosion. In contrast, at 120°C localized corrosion is more pronounced and the surface is covered with individual corrosion pits which are shallow to hemispherical and often occur in cluster-like arrangements. Penetration depths of individual pits can reach up to 40 µm after 10 days. The occurrence of localized corrosion precludes the possibility of measuring the corrosion rate by means of uniform surface retreat. The observed type of corrosion is somewhat reminiscent of classical passivating metals (e.g. stainless steel) undergoing pitting corrosion.

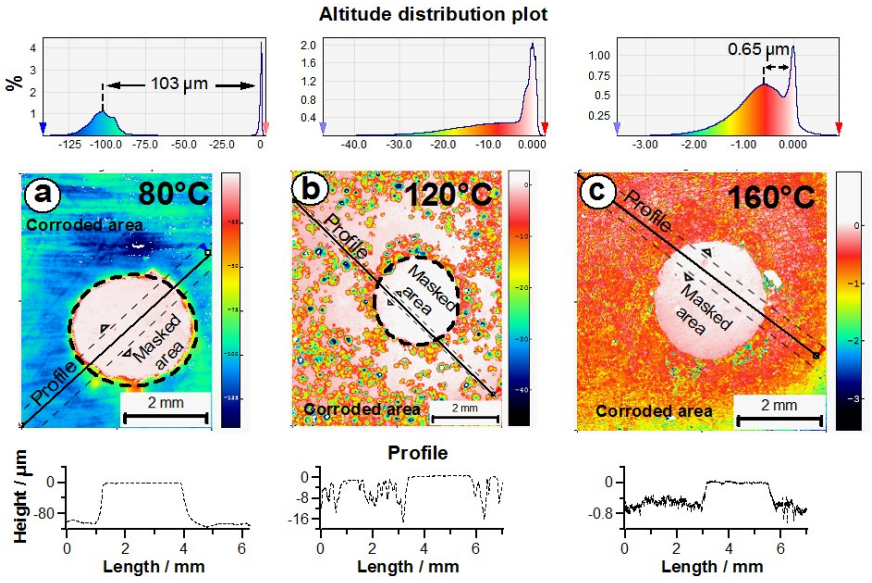

Figure 1 *(left) Vertical scanning interferometry (VSI) images of corroded surfaces (10 days) after corrosion film removal: (a) 80°C, (b) 120°, and (c) 160°C. A profile section (bottom) and an altitude distribution plot (top) are also given for the surfaces.*

Time-dependence of Fe corrosion rates

Using VSI, we measured the volume of Fe dissolved (in mm^3 cm^{-2}) as a function of time and temperature and converted it into µmol cm^{-2} (Fig. 2a). VSI overcomes the limitations of generic time- and area-averaged corrosion

rates that are usually obtained in mass-loss experiments. The dashed lines are the fits (linear for 120°C and logarithmic for 80 and 160°C) showing a very high coefficient of determination R^2. The solid line in Fig. 2a (secondary y-axis) gives the corrosion rate for the 80°C experiment normalized to mm y^{-1} which shows a marked decrease over time but still remains at approx. 5 mm y^{-1}. This exemplifies how misleading average corrosion rates can be and that initial corrosion rates are not representative for long-term estimations.

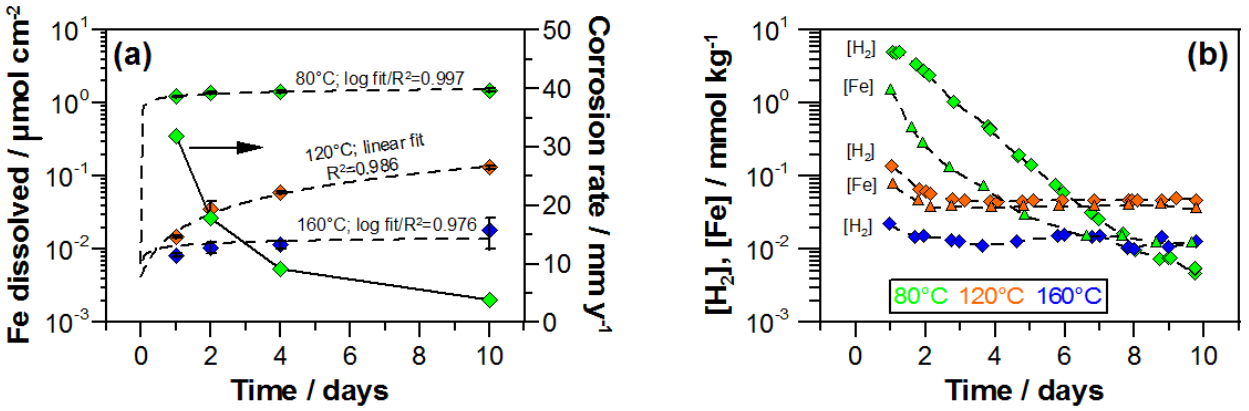

Figure 2 *(a) Fe dissolution rates as a function of time and temperature measured by VSI (dashed lines); also given is the corrosion rate for the 80°C experiments normalized to mm y^{-1} (solid line);(b) ICP-OES and GC results for [Fe] and [H_2] at different temperatures in the effluent.*

At 80°C the Fe dissolution rate is strongly time-variant with the dissolution rate varying over orders of magnitude. Following a logarithmic rate law, it peaks in the initial stage of the experiment and then drops to significantly lower values. The rapid drop of the corrosion rates is due to the development of a continuous corrosion film.

A similar dynamic has also been observed for 160°C and is likely linked to the conditions when uniform corrosion is dominant and localized corrosion features are practically absent. Nonetheless, there is a slight tendency towards parabolic kinetics, a dynamic that has been previously described for magnetite formation in high-temperature environments for which the rate of film growth becomes negligible with time and the film thickness approaches a limiting thickness (Heusler et al., 1990). At 120°C we observe a different behavior and the Fe dissolution rate is constant over time. It appears to be linked to more localized corrosion and we observed an increasing density of localized corrosion pits per area. The Fe dissolution rates in µmol d^{-1} cm^{-2} for the 4-10 day increment have been calculated to be 0.0133 for 80°C, 0.0121 for 120°C, and 0.0012 for 160°C, respectively. Note that the rates for 80 and 120°C are of a similar magnitude, while the rate at 160°C is at least one order of magnitude lower.

$[Fe]_{aq}$ and $[H_2]$ measurements

The effluent was analyzed with respect to dissolved Fe ([Fe]) and gaseous hydrogen ([H_2]; Fig. 2b). The observed dynamic can be well described by the generalized Fe corrosion reaction (eq. 1). As discussed earlier, gaseous H_2 is

the product of the primary cathodic reaction and therefore an index of the rate of the anodic dissolution reaction (King et al., 2014).

At 80°C, high initial corrosion rates generate H_2 at a minimum rate of 12 µmol h^{-1} cm^{-2}. [H_2] reaches a maximum (~5 mmol kg^{-1}) after 24 hours and then decreases exponentially to values below the detection limit of the GC. This is in contrast to the 120 and 160°C experiments where a constant [H_2] is reached at an early stage of the experiment and H_2 production rates are 4.8 and 1.44 µmol day^1 cm^{-2} at 120 and 160°C, respectively.

[Fe] is typically lower than [H_2] because it is partly consumed by the reaction with CO_3^{2-} and HCO_3^- ions to form $FeCO_3$ (Nesic, 2007; Ingham et al., 2015). [Fe] for the 160°C experiment was found to be under the detection limit. Within the first 8 days [Fe] and [H_2] converge towards equimolality. At this point in time the corrosion rate and the rate of film formation are greatly reduced. After 8 days [Fe] even becomes higher than [H_2] (although at very low concentrations). This might indicate that film dissolution is becoming dominant once the corrosion slowed down. The systematic difference between [Fe] and [H_2] at 120 and 160°C is well within the margin of error for the instruments. The discrepancy between [Fe] and [H_2] is a measure of the film formation rate, which is highest at 80°C.

Corrosion films & electrochemical measurements during film formation

Fig. 3 gives SEM images of corrosion films formed after 10 days of exposure at 80, 120, and 160°C, respectively. The 80°C film mostly consists of $FeCO_3$ and reaches a thickness of ~100 µm. It exhibits a duplex structure with a crystalline (faceted) outer $FeCO_3$ layer and an inner layer composed of a skeletal network of Fe_3C impregnated with $FeCO_3$. Hence, the oxygen content of the inner layer is lower as evidenced by EDX analysis. Fe_3C appears brighter in the SEM images and is an undissolved part of the original steel microstructure. The interface between inner and outer layer is therefore likely to be the original steel surface. At higher temperature the thickness of the film decreases. The 120°C film is of intermediate thickness (~10 µm) and appears to have a duplex structure, similar to what we observed at 80°C. The thickness of the 160°C film remains below 3 µm and an internal structure is impossible to identify.

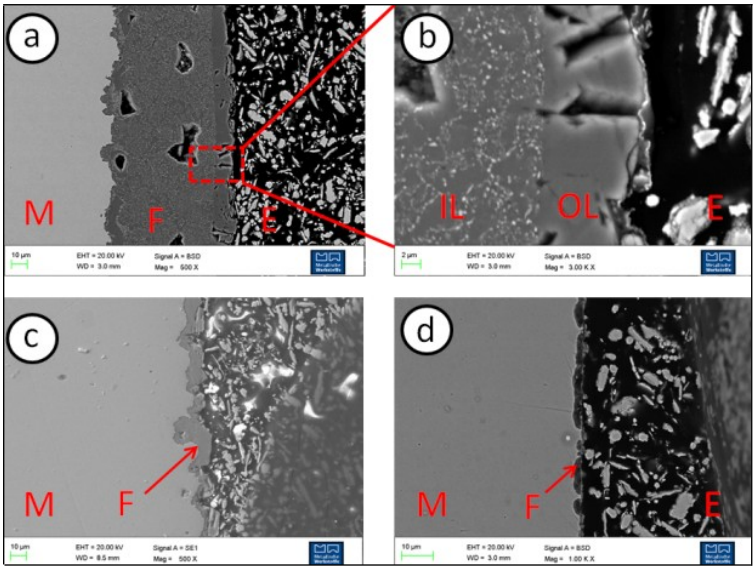

Figure 3 *Cross-sectional SEM-BSD images of corrosion films formed after 10 days at (a) 80°C, (b) 80°C with higher magnification (IL: inner layer, OL: outer layer), (c) 120°C, and (d) 160°C; M, F, and E designate metal, film, and embedding material, respectively.*

Potentiodynamic polarization (PDP)

PDP curves were measured after 1 hour (pre-$FeCO_3$) and 10 days (filmed state) and are given in Fig. 4a. After 1 hour (dashed graphs) the cathodic current density at 80°C is much lower than for 120 and 160°C which could be explained by temperature-accelerated reaction kinetics. All graphs show Butler-Volmer kinetics with Tafel slopes of ~330 mV dec^{-1} which is generally higher than reported elsewhere and suggests a rather complex cathodic reaction pathway for our system.

The anodic branches show no well-defined Tafel region. This is particularly clear for 120 and 160°C where the current increases and then drops to substantially lower values. This shows that in the early stage of the experiment (at 120 and 160°C) an anodic film (presumably Fe_3O_4) forms which precedes the formation of $FeCO_3$. This is conceivable under the experimental conditions since Fe_3O_4 is less soluble than $FeCO_3$ and its formation is thermodynamically favorable. This is consistent with thermodynamic predictions and agrees with results from other studies including TEM work that shows coexisting oxide/carbonate films (Han et al., 2011).

The PDP curves for 80 and 120°C after 10 days are given in Fig. 4a. The corrosion potentials are shifted in the anodic direction which is indicative of the formation of a corrosion film that disproportionally retards the kinetic of the anodic partial reaction. Compared to the pre-film state the anodic current densities are strongly suppressed, reflecting the condition when the metal is covered with a continuous corrosion film. This behavior indicates that the anodic reaction is the rate-limiting step in the corrosion process. The cathodic branch is less affected by the presence of a corrosion film. The cathodic reduction reaction continues relatively unimpeded and is on a similar

order of magnitude at 10 days compared to 1 hour. This is an important observation and suggests that in our corrosion system the anodically and cathodically active site are separated, e.g. by an electrically-conducting corrosion film (see EIS section below).

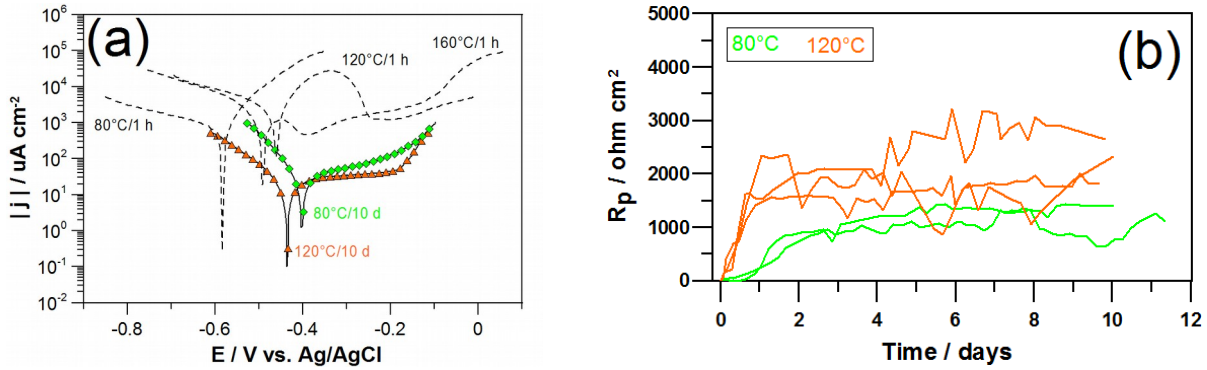

Figure 4 *(a) Potentiodynamic polarization curves after 1 hour (dashed) at 80, 120, and 160°C and 10 days (green and orange) at 80 and 120° respectively; (b) R_p determined in multiple measurements as a function of time.*

Linear polarization resistance (LPR)

Fig. 4 (b) shows the polarization resistance (R_p) over the course of 10-day experiments which is inversely proportional to the instantaneous corrosion rate. However, in order to accurately quantify the corrosion rate using R_p, the anodic and cathodic Tafel slopes have to be either constant or known over time. Particularly the anodic reaction, however, is not governed by Tafel behavior due to the presence of a corrosion film. R_p is therefore only a vague index of the rate at which corrosion occurs but can indicate whether or not the system reached a steady state.

The initial pre-film R_p at all temperatures is around 15 Ω cm^2, which correlates with very high corrosion current densities on the order of several mA cm^{-2}. At 80°C R_p remains low and even decreases in the first 20 hours. We attribute this initial increase in corrosion rate to the preferential dissolution of ferrite which exposes an ever-increasing surface area of electrochemically active Fe_3C. This aspect will be discussed in more detail in the EIS section. Afterwards R_p increases moderately to reach steady-state conditions after approx. 4 days. At 120°C R_p rapidly increases which indicates a faster interfacial reaction that produces a corrosion film (Han et al., 2011). The pseudo-passive state displayed in the anodic branches of the PDP curves is reached in the first hours of the experiment. At 120°C R_p is subject to fluctuation due to localized corrosion, as evidenced by VSI. Area-normalized R_p values can therefore only be interpreted with caution due to high localized dissolution rates.

Electrochemical impedance spectroscopy (EIS)

EIS as one component of electrochemical analysis is a powerful technique to extract mechanistic information about a corroding system. However, interpreting EIS data and attributing physical meaning to the circuit components is very challenging and often not well documented. This paper, therefore, provides instructional advice on how to

approach EIS data and guidance for the development of appropriate physical models to extract system-relevant data.

Qualitative analysis

Here we showcase the EIS results for immersion times of 5 hours and 10 days to contrast the different impedance behavior that is related to the formation of a corrosion film. In addition, impedance spectra from the early stage of an experiment enable us to assign impedance features to specific reactions and help us to trace changes of the impedance over time.

The impedance spectrum measured after 5 hours is given in the inset of Fig. 5a. It consists of two partially-overlapping capacitive arcs and one inductive arc (at very low frequencies) and represents the case of high initial dissolution of a bare metal surface. That the surface is bare is reflected by the fact that the horizontal diameters of the arcs are very low (on the order of tens of ohm cm^2). The capacitive arc at intermediate frequencies and the inductive loop at low frequencies (LF) are commonly associated with the Fe oxidation reaction in an acidic or mildly acidic electrolyte, such as in our experiments (Almeida et al., 2017; Barcia & Mattos, 1990; Keddam et al., 1981). Inductive behavior is assigned to a multistep charge-transfer reaction that involves an adsorbed intermediate product. The high-frequency (HF) arc is assigned to the hydrogen reduction reaction (HRR). In fact, the HF arc becomes even smaller after 5 hour before it significantly increases in size after ~20 hours. The nature of the time dependency of the arc's size is attributed to the variation of the rate of the HRR with changes in the amount of cathodically-active sites (Farelas et al., 2010; Zhang & Cheng, 2009).

The impedance behavior after 10 days is given in the Nyquist representation in Fig. 5a. The spectrum consists of two overlapping capacitive arcs. The impedance magnitude increased strongly and the shape of both arcs became more depressed (center below the x-axis), which is indicative of "non-ideal" capacitive behavior. As in our analysis of the EIS at 5 h, the HF capacitive arc is assigned to the HRR and the LF arc is associated with the oxidation reaction. The LF arc is rather ill-defined because its HF end is masked by the overlapping HF arc associated with the HRR. The LF end is absent because our measurements were truncated at a LF limit of 2.5 mHz.

Additional information is obtained from the Bode representation in Fig. 5b. It shows that after 5 hours the plot of phase angle φ is very symmetrical over a wide range of frequencies (except for the lowest frequencies measured) and exhibits a rather sharp peak. After 10 days the peak has broadened considerably and the plot is noticeably asymmetric. The HF end of the plot of the modulus is almost horizontal and the phase angle approaches 0° representing mostly resistive behavior (typically the solution resistance).

For an enhanced analysis Z' and -Z'' versus log f were plotted in Fig. 5c. After 10 days the plot of the imaginary component contains two distinct slopes that are dominant over a wide frequency range, ~-0.77 in the high to intermediate frequency range and ~-0.2 in the LF range below 1 Hz. Note that the HF end of the imaginary component is not obscured by the solution resistance which drives the plots of the modulus and the real component

to horizontal lines. Our data shows that the straight line (slope ~-0.77) observed in the intermediate frequency range (3 Hz – 3 kHz) does not extend to the maximum frequency of 100 kHz (dashed ellipse) on account of the HF impedance of our reference electrode (Mansfeld et a., 1988).

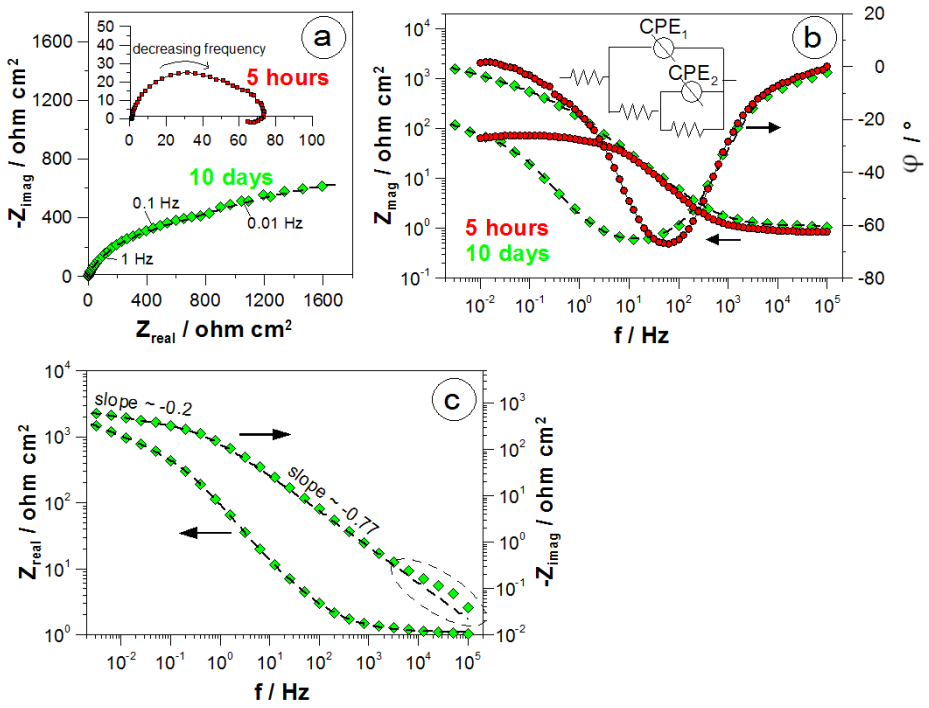

Figure 5 *(a) Bode plot (including phase angle) and (b) Nyquist plot for a 80°C experiment after 10 days; the equivalent circuit used for the analysis is given in the inset; (c) Z' and -Z'' plotted against the log f*

Equivalent circuit (EC) analysis

Conceptually, corrosion at the OCP is the combination of an anodic reaction (metal dissolution) and a cathodic reaction (electrolyte reduction). The system's impedance therefore consists of an anodic impedance in parallel with a cathodic impedance plus a solution resistance in series. Based on the qualitative analysis above, we propose a two time constant EC (inset of Fig. 5b) as one that simulates the impedance behavior of our electrochemical system after 10 days. The fits are given as black dotted lines in Fig. 5a-c and are in good agreement with the experimental data. Generally, the phase angle is more sensitive to system parameters than the impedance magnitude and better suited to evaluate reproducibility and validity of EC models.

The impedance spectrum suggests the presence of two constant phase elements (CPE) that are associated with the oxidation and the reduction reactions. A CPE has the mathematical form $Z_{CPE} = Z_0 (i\omega)^{-\alpha}$, where Z_0 is a pre-factor, i=$\sqrt{-1}$, $\omega=2\pi f$, and α is a dispersion coefficient. Note that Z_0 does not have the units of capacitance (F cm^{-2}), but instead Ω^{-1} cm^{-2} s^{α}. The α values are obtained by EC modeling or from the -log Z_{im} vs. log f plot (Fig. 5c) where they appear as the slopes of the linear segments, -0.77 and -0.2, respectively. There are a number of potential causes of

CPE behavior and simply including a CPE in an EC does not provide insight into the mechanisms of the reactions (Orazem & Tribollet, 2017). Mechanistic insight requires that the CPE be assigned to a specific phenomenon.

The initial increase in corrosion rate with time is attributed to the increase in rate with time of the HRR. The preferential dissolution of ferrite exposes an ever-increasing surface area of Fe_3C, which is the site of the HRR. After approximately one day the high concentration of ferrous ions produced by the oxidation reaction exceeds the solubility limit and a surface film of $FeCO_3$ is formed. It is worth noting that the critical oversaturation for nucleation of crystalline $FeCO_3$ from an amorphous precursor can be exceedingly high (Ingham et al., 2015).

Analysis of EIS complements the results of the corrosion rate measurements and the SEM observations and advances our mechanistic understanding of the corrosion system. CPE-like behavior is attributed to the presence of a porous corrosion film mainly composed of $FeCO_3$ and Fe_3C, as observed in similar environments. The two most important properties of the film's constituents are: (1) $FeCO_3$ is a very poor electron conductor and is electrochemically inert; (2) Fe_3C is an excellent electronic conductor (Lee & Simkovich, 1987) and provides a surface on which the HRR takes place (Dong et al., 2017; Ferhat et al., 2014; Nesic & Lunde, 1994). In contrast to Fe_3C, Fe is known as a relatively poor surface for the HRR. In multiple tests the value of α at high frequencies exhibited some scatter and ranged from 0.6 to 0.8 (-0.77 in Fig. 5c). Diffusive impedances, such as that associated with ion transport through a solid surface film and ion transport through a stagnant electrolyte, have $\alpha = 0.5$. Ion diffusion in irregularly shaped pores (i.e., non-cylindrical pores) is associated with values of α that are a few tenths larger or smaller than 0.5, dependent on the pores shape (Cooper et al., 2017). We hypothesize that once the ferrite phase is preferentially corroded the Fe_3C forms a naturally porous structure. Once the Fe_3C is partially covered by a surface film of $FeCO_3$, the HRR now occurs on a porous surface, which explains the values of α of 0.6 to 0.8.

In multiple tests the value of α at low frequencies ranged from 0.2 to 0.3 (in Figure 5c the value is ~0.2). The LF values of α are associated with the oxidation of Fe covered with a surface film of $FeCO_3$ that contains irregularly shaped pores. We hypothesize that the very different value of α at low frequencies compared to high frequencies is caused by the different geometries of pores in the films of $FeCO_3$ that form on the ferrite phase versus the film that forms on the Fe_3C.

Implications for geotechnical applications

We have illustrated the dynamics of corrosion and corrosion film formation under conditions relevant to geotechnical applications. Temperature is a key parameter that impacts both the kinetics of corrosion and the type of corrosion. Both aspects are critical for any long-term prediction of material integrity, particularly in NWD where the highest safety requirements are mandated.

At 80°C corrosion rates over time show a logarithmic trend. Uniform corrosion is prevalent and corrosion rates eventually drop significantly. However, strong H_2 generation in the initial stage might lead to pressure build-up and cause problems for impermeable rock formations or engineered barriers in NWD. At 120°C corrosion is more

localized and corrosion rates follow a linear trend over time. This suggests that relatively high corrosion rates are maintained due to an autocatalytic process possibly taking place in the pit bottom. This less predictable type of corrosion is a major concern for operators in safety-critical applications. The least severe corrosion conditions are found at 160°C where corrosion rates are at least one order of magnitude lower and uniform corrosion is prevalent.

The limitations of laboratory tests to predict corrosion in real-world applications should be clearly pointed out. Other factors, such as high flow rates or microbially-influenced corrosion at lower temperatures, might play an important role. For instance, it was found that Fe-reducing bacteria can substantially enhance corrosion rates by destabilizing magnetite at temperatures below 100°C (Schütz et al., 2015; Spark et al., 2017). Mixed cation/anion solutions, like most natural waters, might also lead to a different outcome with respect to corrosion and particularly to film formation (Lee et al., 2006).In NWD, γ radiation originating from the spent nuclear fuel may produce powerful oxidants by radiolysis ($HO\cdot_{aq}$, H_2O_2) that enhance metal corrosion substantially (Björkbacka et al., 2016).

Acknowledgments

Laboratory work has been conducted at the Hydrothermal Laboratory (Lawrence Berkeley National Laboratory) using funding granted by the German Research Foundation (DFG; Grant No. MU 3821/2-1) in form of a 2-year postdoctoral fellowship. We thank the five anonymous reviewers for their valuable feedback.

References

Almeida, T. C.; Bandeira, M. C. E.; Moreira, R. M.; Mattos, O. R., 2018. Discussion on “Electrochemistry of CO_2 corrosion of mild steel: Effect of CO2 on iron dissolution reaction” by A. Kahyarian, B. Brown, S. Nesic, [Corros. Sci. 129 (2017)]. Corrosion Science 133, 417-422.

Almeida, T. d. C.; Bandeira, M.C.E.; Moreira, R.M.; Mattos, O.R., 2017. New Insights on the Role of CO2 in the Mechanism of Carbon Steel Corrosion. Corrosion Science 120, 239-250.

Banas, J.; Lelek-Borkowska, U.; Mazurkiewicz, B.; Solarski, W., 2007. Effect of CO_2 and H_2S on the composition and stability of passive film on iron alloys in geothermal water. Electrochimica Acta 52, 5704-5714.

Barcia, O.E.; Mattos, O.R., 1990. The Role of Chloride and Sulfate Anions in the Iron Dissolution Mechanism Studied by Impedance Measurements. Electrochmica Acta 35, 1003-1009.

Björkbacka, A.; Magnus Johnson, C.; Leygraf, C.; Jonsson, M., 2016. Role of the Oxide Layer in Radiation-Induced Corrosion of Copper in Anoxic Water. J. Phys. Chem. C 120, 11450−11455.

Blengino, J. N.; Keddam, M.; Labbe, J. P.; Robbiola, L., 1995. Physico-Chemical characterization of corrosion layers formed on iron in a sodium carbonate-bicarbonate containing environment. Corrosion Science 37, 621-643.

Choi, Y.-S.; Nesic, S.; Young, D., 2010 Effect of Impurities on the Corrosion Behavior of CO_2 Transmission Pipeline Steel in Supercritical CO_2-Water environments. Environ. Sci. Technol. 44, 9233-9238.

Cooper, S.J.; Bertei, A.; Finegan, D.P.; Brandon, N.P., 2017. Simulated Impedance of Diffusion in Porous Media. Electrochimica Acta 251, 681-689.

Dong, J.; Hao, X.; Wei, J.; Ke, W., 2017. Study on the Galvanic Corrosion of Ferrite-Pearlite Steel and Its Control Under an Acid Environment. Journal of Physical Chemistry and Biophysics 7, 68.

Ellis, A. J.; Mahon, W. A. J., 1977. Chemistry and Geothermal System; Academic Press: New York.

Farelas, F.; Galicia, M.; Brown, B.; Nesic, S.; Castaneda, H., 2010. Evolution of dissolution processes at the interface of carbon steel corroding in a CO2 environment studied by EIS. Corrosion Science 52, 509-517.

Ferhat, M.; Benchettara, A.; Amara, S.E.; Najiar, D., 2014. Corrosion Behavior of Fe-C Alloys in a Sulfuric Medium. J. Mater. Environ. Sci. 5, 1059-1068.

Feron, D.; Crusset, D.; Gras, J.-M., 2008. Corrosion issues in nuclear waste disposal. Journal of Nuclear Materials 379, 16-23.

Gao, M.; Pang, X.; Gao, K., 2011. The growth mechanism of CO_2 corrosion product films. Corrosion Science 53, 557-568.

Han, J.; Nesic, S.; Yang, Y.; Brown, B. N., 2011. Spontaneous passivation observations during scale formation on mild steel in CO_2 brines. Electrochimica Acta 56, 5396-5404.

Heusler, K. E.; Kusian, B.; McPhail, D., 1990. Kinetics of the Corrosion of Iron in Aqueous Electrolytes at Temperatures up to 300°C. Ber. Bunsenges Phys. Chem. 94, 1443-1449.

Ingham, B.; Ko, M.; Laycock, N.; Kirby, N. M.; Williams, D. E., 2015. First stages of siderite crystallization during CO_2 corrosion of steel evaluated using in situ synchroton small- and wide-angle X-ray scattering. Faraday Discussions 180, 171-190.

Kahyarian, A.; Brown, B.; Nesic, S., 2017. Electrochemistry of CO_2 corrosion of mild steel: Effect of CO_2 on iron dissolution reaction. Corrosion Science 129, 146-151.

Keddam, M.; Mattos, O. R.; Takenouti, H., 1981. Reaction Model for Iron Dissolution Studied by Electrode Impedance. Journal of the Electrochemical Society 128, 266-274.

King, A. D.; Birbilis, N.; Scully, J. R., 2014. Accurate Electrochemical Measurement of Magnesium Corrosion Rates; a Combined Impedance, Mass-Loss and Hydrogen Collection Study. Electrochimica Acta 121, 394-406.

Landolt, D., 2007. Corrosion and Surface Chemistry of Metals; EPFL Press: Lausanne, 2007.

Lee, C. T.; Qin, Z.; Odziemkowski, M.; Shoesmith, D. W., 2006. The influence of groundwater anions on the impedance behavior of carbon steel corroding under anoxic conditions. Electrochimica Acta 51, 1558-1568.

Lee, M.C.; Simkovich, G., 1987. Electrical Conduction Behavior of Cementite, Fe3C," Metallurgical and Materials Transactions A 18, 485-486.

Linter, B. R.; Burstein, G. T., 1999. Reactions of pipeline steels in carbon dioxide solutions. Corrosion Science 41, 117-139.

Mansfeld, F.; Lin, S.; Chen, Y.C.; Shih, H., 1988. Minimization of High Frequency Phase Shifts in Impedance Measurements. Journal of the Electrochemical Society 135, 906-907.

Mundhenk, N.; Huttenloch, P.; Bäßler, R.; Kohl, T.; Steger, H.; Zorn, R., 2014. Electrochemical study of the corrosion of different alloys exposed to deaerated 80 °C geothermal brines containing CO_2. Corrosion Science 84, 180-188.

Mundhenk, N.; Huttenloch, P.; Kohl, T.; Steger, H.; Zorn, R., 2013 Metal corrosion in geothermal brine environments of the Upper Rhine graben – Laboratory and on-site studies. Geothermics 46, 14-21.

Mundhenk, N.; Huttenloch, P.; Sanjuan, B.; Kohl, T.; Steger, H.; Zorn, R., 2013. Corrosion and scaling as interrelated phenomena in an operating geothermal power plant. Corrosion Science 70, 17-28.

Nesic, S., 2007. Key issues related to modelling of internal corrosion of oil and gas pipelines – A review. Corrosion Science 49, 4308-4338.

Nesic, S.; Lunde, L., 1994. CO2 Corrosion of Carbon Steel in Two-Phase Flow, Corrosion 50, 717-727.

Orazem, M.E.; Tribollet, B., 2017. Electrochemical Impedance Spectroscopy; John Wiley & Sons, Inc.

Parkhurst, D. L.; Appelo, C. A. J., 1999. User's guide to PHREEQC (Version 2): A Computer Program for the Speciation, Batch-Reaction, One-Dimensional Transport, and Inverse Geochemical Calculations; Water Resources Investigations Report 99-4259; U.S. Geological Survey: Reston, VA, 1999.

Pfennig, A.; Bäßler, R., 2009. Effect of CO_2 on the stability of steels with 1% and 13% Cr in saline water. Corrosion Science 51, 931-940.

Pollet-Villard, M.; Daval, D.; Ackerer, P.; Saldi, G.D.; Wild, B.; Knauss, K.G.; Fritz, B., 2016. Does crystallographic anisotropy prevent the conventional treatment of aqueous mineral reactivity? A case study based on K-feldspar dissolution kinetics. Geochimica et Cosmochimica Acta 190, 294-308.

Scheiber, J.; Seibt, A.; Birner, J.; Cuenot, N.; Genter, A.; Moeckes, W., 2014. Barite Scale Control at the Soultz-sous-Forets (France) EGS Site. Proceedings 38th Workshop on Geothermal Reservoir Engineering Stanford University 2014.

Schlegel, M. L.; Bataillon, C.; Blanc, C.; Prêt, D.; Foy, E., 2010. Anodic activation of iron corrosion in clay media under water-saturated conditions at 90 degrees C: characterization of the corrosion interface. Environ. Sci. Technol. 44(4), 1503-1508.

Schütz, M. K.; Schlegel, M. L.; Libert, M.; Bildstein, O., 2015. Impact of Iron-reducing Bacterial on the Corrosion Rate of Carbon Steel under Simulated Geological Disposal Conditions. Environ. Sci. Technol. 49, 7483-7490.

Soltis, J., 2015. Passivity breakdown, pit initiation and propagation of pits in metallic materials – Review. Corrosion Science 90, 5-22.

Spark, A. J.; Law, D. W.; Ward, L. P.; Cole, I. S.; Best, A. S., 2017. Effect of Pseudomonas fluorescens on Buried Steel Pipeline Corrosion. Environ. Sci. Technol. 51, 8501-8509.

Szklarska-Smialowska, Z., 1986. Pitting Corrosion of Metals; NACE, 1986.

Tanupabrungsun, T.; Brown, B.; Nesic, S., 2013. Effect of pH on Corrosion of Mild Steel at Elevated Temperatures. NACE Corrosion 2013, 2348, 1-11.

Zhang, G. A.; Lu, M. X.; Qiu, Y. B.; Guo, X. P.; Chen, Z. Y., 2012. The Relationship between the Formation Process of Corrosion Scales and the Electrochemical Mechanism of Carbon Steel in High Pressure CO_2-Containing Formation Water. Journal of the Electrochemical Society 159(9), 393-402.

Zhang, G.A.; Cheng, Y.F., 2009. On the Fundamentals of Electrochemical Corrosion of X65 Steel in CO2-Containing Formation Water in the Presence of Acetic Acid in Petroleum Production. Corrosion Science 51, 87-94.